https://doi.org/10.5194/egusphere-2025-5650
Preprint. Discussion started: 3 December 2025

# Unexpected land-surface warming following a low-to-moderate forcing hypothetical nuclear war

Anson Ka Hei Cheung[1], Paul J. Kushner[1], Francesco S. R. Pausata[2], Zhihong Zhuo[2], Marguerite L. Brown[2]

[1]Department of Physics, University of Toronto

[2]Department of Earth and Atmospheric Sciences, University of Quebec in Montreal
*Correspondence to*: Anson Ka Hei Cheung (anson.cheung@mail.utoronto.ca), Paul J. Kushner (paul.kushner@utoronto.ca)

**Abstract.** Nuclear conflicts could ignite intense urban fires that inject considerable amounts of black carbon (BC) into the upper atmosphere, with the potential to disrupt global climate. While uncertainties in the total BC injection remain large, relatively few modeling studies and limited model diversity have explored the climatic response to low-to-moderate BC injections, leaving key aspects of their climate impact poorly understood. Here, we investigate the climate response to a set of low-to-moderate forcing scenarios (12 to 24 Tg BC) – roughly one-tenth to one-fifth the strength of the standard high-end cases – using the Canadian Earth System Model version 5. Consistent with previous work, we find prolonged global reductions in surface temperature and precipitation, driven by decreased downwelling shortwave radiation at the surface and increased atmospheric stability. Unexpectedly, however, a transient surface warming develops in the first boreal summer following a boreal-winter injection, linked to reduced net longwave and turbulent fluxes. Precipitation remains suppressed because of enhanced stability. The transient warming is most pronounced for the lowest forcing cases, indicating a nonlinear response across the forcing range. These results underscore the need for broader multi-model assessments and systematic exploration across a wider range of scenarios, given their potential for complex, societally relevant outcomes.

## 1 Introduction

Although the global nuclear arsenal has shrunk since the Cold War, global society is still threatened by potential nuclear conflict due to rising geopolitical tension and the proliferation of regional nuclear powers. In addition to local damage and health effects at the locations of nuclear detonation (Lucas et al., 1990; Solomon & Marston, 1986), regional nuclear conflicts can have global climatic effects, including stratospheric warming, surface cooling, and reduced precipitation (Coupe et al., 2019; Robock et al., 2007a; Toon et al., 2007) as well as reduction in the ozone layer thickness (Mills et al., 2008; Mills et al., 2014).

The global effects stem from firestorms that are triggered at targeted urban and industrial centers. The firestorms can induce convection capable of injecting a great amount of inorganic and organic carbon into the upper troposphere - lower stratosphere (UTLS) (Tarshish & Romps, 2022; Toon et al., 2007). Climate modeling studies have shown that the carbonaceous aerosol can heat the upper atmosphere and cool the Earth's surface by increasing the absorption of solar radiation aloft (Pausata et al., 2016; Robock et al., 2007a). Upon local heating, the aerosol-laden air becomes buoyant and rises to a higher altitude. This 'self-lofting' prolongs the aerosol residence time (Johnson & Haywood, 2023; Malone et al., 1985; Ohneiser et al., 2023). In a hypothetical case of a full-scale nuclear exchange between the United States and Russia, a UTLS injection of a large amount of black carbon (BC) would drive unprecedented stratospheric warming and surface cooling at a global scale (Robock et al., 2007a). The surface cooling may lead to crop failure and famine, slowing down societal recovery (Xia & Robock, 2013; Xia et al., 2015, Xia et al., 2022). Precipitation would also be reduced globally due to reduction in solar heating, evaporation, and convection. Disruption of stratospheric chemistry would lead to ozone depletion via various mechanisms even for a modest BC injection in a nuclear conflict between India and Pakistan (Mills et al., 2008; Mills et al., 2014). The resulting increase in surface UV radiation could damage human health and ecosystems on a global scale.

Both the amounts of BC emission and UTLS injection are highly uncertain. Taking into account the uncertainties in the BC-emission factors of flammable materials and the quantities to be burned, Turco et al. (1990) considered a wide range of plausible BC emissions, from 20 to 290 Tg, that could arise as a result of a full-scale nuclear exchange involving the North Atlantic Treaty Organization (NATO) and Warsaw Pact nations. Beside emission factor uncertainty, variations in local meteorology, modern warfare tactics, and rubblization of fuels all contribute to the uncertainty in the total amount of BC injected into UTLS (Glasstone & Dolan, 1977; NASEM, 2025; Tarshish & Romps, 2022). However, for this full-scale nuclear exchange scenario, most studies considered a UTLS injection of 150 Tg BC as a standard scenario (Bardeen et al., 2021; Coupe et al., 2019; Robock et al., 2007a), with little attention given to low-to-moderate forcing scenarios involving smaller BC injections from nuclear-war fires. Yet a nuclear conflict would not necessarily entail the use of the entire arsenal; assessing the climate effects of such partial or regional exchanges is therefore essential to capture the plausible range of outcomes. In this context, smaller injection estimates on the order of 10-25 Tg BC become particularly relevant, as they represent plausible outcomes of limited nuclear exchanges rather than full-scale global war. For instance, a UTLS injection of 10-25 Tg BC for the USA-Russia scenario would be small compared to the 150 Tg load in Coupe et al. (2019) and Robock et al. (2007a) but still extreme relative to natural forcing or recent forest fires. For comparison, the 2019 Australian wildfires emitted 0.9 Tg of smoke into the stratosphere, of which 2.5% was BC and the remainder mostly organic carbon (OC) (Yu et al., 2021). Model calculations estimated a statistically significant warming and ozone depletion in the southern hemispheric midlatitude stratosphere for 6 months as a result of these wildfire emissions. Compared to typical wildfires, the smoke injected into the UTLS would have a higher BC-to-OC ratio due to lower oxygen content in large-scale urban fires (Shemwell & Levendis, 2000; Tewarson, 2002; Toon et al., 2007). Therefore, it is a pertinent question to ask how the climate response might differ under a low-to-moderate BC injection scenario.

In this study, we look into the climate response to relatively weak BC injection with the use of an atmosphere-ocean coupled model, the Canadian Earth System Model version 5.1 (CanESM5; Swart et al., 2019). This is the first time CanESM is used for the study of nuclear war fire emissions. Its independent development from other climate models helps characterize model uncertainty. Although it is a low top model with a coarse stratospheric representation and a lack of stratospheric chemistry and aerosol model, it is a workhorse ESM that has been extensively used in many climate simulations studying anthropogenic climate change effects stemming from the Coupled Model Intercomparison Project phase 6 (CMIP6; Eyring et al., 2016, Samset et al., 2025). We test the sensitivity of the response by varying the total BC injection around the low end of the estimated emission in a full-scale nuclear exchange, between 12 and 24 Tg. This study represents an effort to investigate this model's climate response to such forcing before the CanESM system moves to subsequent more advanced versions with updates to the aerosol scheme. In this study, we find a previously undocumented transient ‘whiplash’ as the model transitions to a nuclear winter state through an early summertime warming response, unexpectedly strong high-latitude responses to stratospheric BC injection, and other effects. This relatively weak but plausible forcing scenario bears investigating in other models.

In Section 2, we provide a description of the model used and parameterizations of relevant processes, as well as the experimental set-up. In Section 3, we investigate the climate response to different amounts of BC emission in the low-to-moderate forcing scenarios. In Section 4, we summarize the results and discuss the potential implications and future work.

## 2 Methods

### 2.1 Model description

We conduct the simulations using the Canadian Earth System Model version 5.1 (CanESM5; Swart et al., 2019), which contains an atmosphere component that incorporates a land model, coupled with the ocean model NEMO (Madec & the NEMO team, 2012). The atmosphere component of CanESM5 is the Canadian Atmospheric Model version 5 (CanAM5) with a bulk aerosol scheme employed (Cole et al., 2023). It is a T63 spectral dynamical core model (2.8° horizontal resolution) with 49 vertical layers with layer thickness that increases monotonically from approximately 100 m at the surface to 2 km at about 1 hPa, which is the upper bound. The number of vertical levels has been increased from its predecessor, CanAM4 (von Salzen et al., 2013), to match those employed by the Canadian Middle Atmosphere Model (Scinocca et al., 2008), but the stratosphere is still coarsely represented, with 18 levels from about 300 hPa to 10 hPa. The quasi-biennial oscillation is not simulated by CanAM5. Biases in stratospheric temperature and zonal wind are reduced in CanAM5 relative to CanAM4 (Cole et al., 2023). Despite having a low model top, CanESM5 has been used in the framework of understanding climate perturbations involving dynamical and radiative coupling of the troposphere to the lower stratosphere. For example, it has been used in the Model Intercomparison Project on the climatic response to volcanic forcing (VolMIP; Zanchettin et al., 2016), which is an endorsed contribution to the CMIP6. It also has good performance in realizing the Arctic sea-level pressure response to sudden stratospheric warming among CMIP6 models when compared to reanalysis (Dai et al., 2024), suggesting that it simulates stratosphere-troposphere interactions adequately for our sensitivity study.

CanAM5 employs bulk cloud microphysical parameterizations that depend on the mean water content and other moments of droplet size distributions (von Salzen et al., 2013). The autoconversion, cloud liquid water content, and cloud lifetime depend on a cloud droplet number concentration that is a function of sulphate concentration (Ghan et al., 2013; Wood, 2005). The latter parameterization represents what is known as the second aerosol indirect effect. CanAM5 also parameterizes the BC semi-direct radiative effect as a perturbation to existing liquid cloud optical properties according to the volume fraction of BC to cloud water (Li et al., 2013). The cloud processes are limited to pressures greater than 10 hPa given the uncertainty in the applicability of the parameterizations at high altitudes. Aerosols that are considered in CanAM5 include sulfate, BC, OC, sea salt, and mineral dust. Hydrophilic BC, hydrophilic OC, and sulfate are assumed to be internally mixed in CanAM5 and have a refractive index that depends on the fraction, effective radius, and effective variance of each component aerosol, as well as the relative humidity (Wu et al., 2018). CanAM5 does not take into account the aerosol number for determining gravitational settling rate, unlike some other models that have been used for the climate impact study of nuclear conflicts such as NorESM1-M (Pausata et al., 2016) and CESM2-WACCM6 (Gettelman et al., 2019).

Aerosols are removed from the atmosphere by dry and wet deposition. In CanAM5, the dry deposition flux is parameterized based on near-surface aerosol concentration and a specified dry deposition velocity that depends on the type of tracer and the local surface condition (Croft et al., 2005; Lohmann et al., 1999). For wet deposition, CanAM5 includes below-cloud scavenging for stratiform clouds and in-cloud scavenging for both stratiform and convective clouds. The below-cloud scavenging rate depends on the precipitation rate, whereas the in-cloud scavenging rates depend on the precipitation formation rate. The snow-darkening effect of BC deposition is also included in CanAM5. The total BC deposition flux is used to calculate the BC mass budget in snow layer, whose snow albedo is parameterized as a function of BC mass mixing ratio in snow, snow water equivalent, snow grain size, underlying surface albedo, and solar zenith angle (Namazi, et al., 2015).

### 2.2 Experimental design

We generate an ensemble with an injection of 20 Tg of BC (hereafter as BC20), consisting of 15 ensemble members. To generate the ensemble members, we select different years from a 100-year pre-industrial control simulation as the initial years (Eyring et al., 2016). All selected years are at a neutral state of the El Niño-Southern Oscillation (ENSO) in January to avoid potential ENSO imprint on the simulated responses. To test the sensitivity of the global mean climate response to BC aerosol, we generate 3 additional ensembles, each consisting of 3 ensemble members, with an injection of 12 Tg, 16 Tg, and 24 Tg of BC (hereafter as BC12, BC16, and BC24), respectively. While we were interested in extending beyond this limit, we have found that the model was rendered unstable for forcings greater than about 40 Tg and that the climate response exhibits unexpected features even in the low-to-moderate forcing scenarios. All injected BC particles are assumed hydrophilic from the start. As in previous studies, the particles are injected uniformly between 300 to 150 hPa over the United States and Russia at a constant rate over 1 week, starting from January 1st. To evaluate the long-term response, each simulation is run for 20 years from the first day of emission.

## 3 Results

### 3.1 BC burden response and impacts on global shortwave and longwave radiation

For all cases, more than two-thirds of the BC burden stays under the overworld, which is defined as the domain above the 380 K potential temperature surface (around 15 km above the Earth’s surface) (Holton et al., 1995), and gets removed in the first year (Fig. 1a). The BC burden in the lower atmosphere (under the 380 K potential temperature surface) is relatively greater in the first year before getting removed, which is important for the shorter-term climate

https://doi.org/10.5194/egusphere-2025-5650
Preprint. Discussion started: 3 December 2025

response. The overworld burden for BC12 attains its maximum at 2.0 Tg in first year June, while the overworld burden for BC24 attains its maximum at 5.2 Tg in the same month, so doubling the injection from 12 Tg to 24 Tg results in more than 2.5 times more BC being lofted into the overworld. After reaching the maximum burden in the overworld, the overworld BC mass e-folding time, which is defined by the time it takes for the burden to reach $e^{-1}$ of its maximum, for BC16, BC20, and BC24 is estimated between 3 years and 6 months, and 3 years and 8 months, while the mass e-folding time for BC12 is 3 years and 3 months. In the lower atmosphere, the mass e-folding time is 3 months for all 4 cases. Throughout the simulated period, the fraction of remaining mass of BC is greater in the larger-forcing scenario (Fig. 1b). The nonlinear dependence of early-stage BC lofting on the total mass of injection influences the long-term climate response since the overworld burden has a much longer residence time compared to lower atmospheric burden.

https://doi.org/10.5194/egusphere-2025-5650
Preprint. Discussion started: 3 December 2025

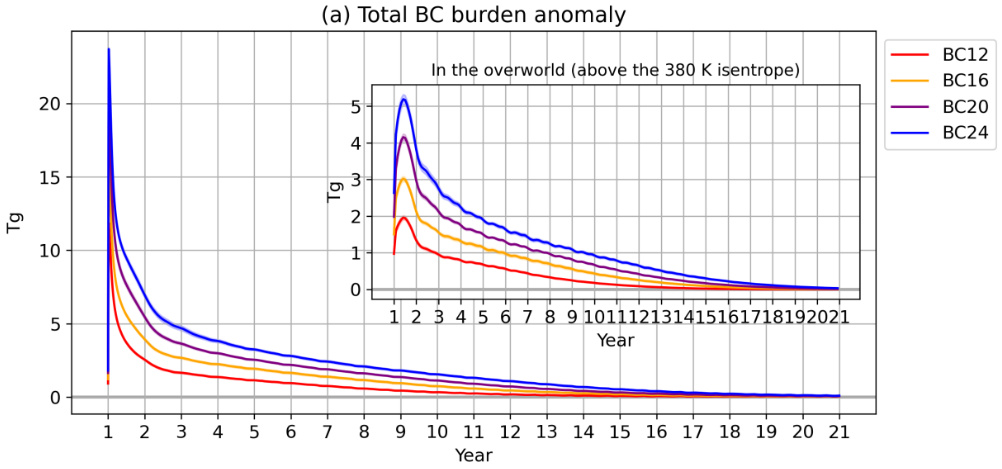

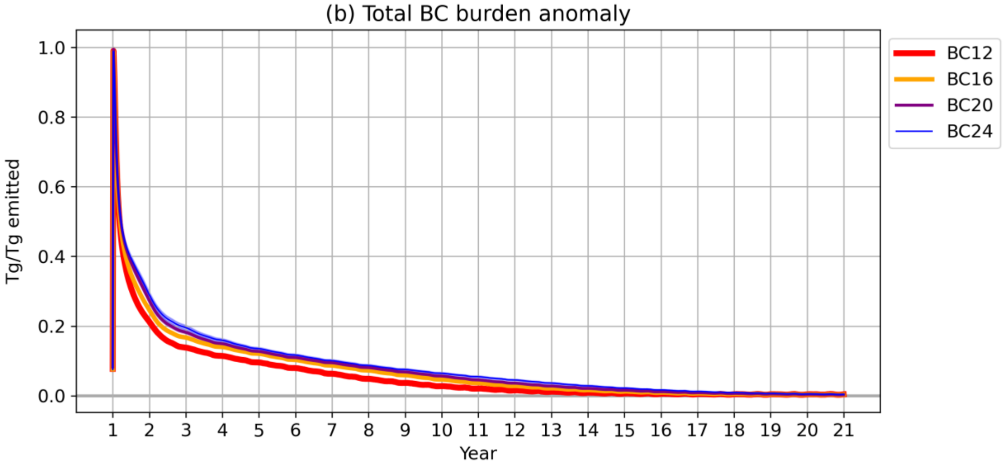

**Figure 1.** Daily averaged BC burden anomalies relative to the control simulation (a) in the atmosphere, (inset of a) in the overworld domain, and (b) in the atmosphere per Tg of emitted BC. Shading indicates the standard error of the mean. In (b), the lines for different ensembles are varied in thickness to show where they overlap.

As will be shown, the climate responses exhibit distinct behaviours during January to February (JF) of first year, June to August (JJA) of first year, and years 6 to 15. The temporal means of the climate responses for these primary periods of interest will be highlighted throughout this section (Table 1).

Absorption of solar radiation by BC reduces surface downwelling shortwave radiative flux (DSRF). The response in the global mean surface DSRF reaches a minimum in two months following the UTLS injection BC (Fig. 2a). The response is –14.80 W m$^{-2}$ and –26.96 W m$^{-2}$ in first year January and February for BC12 and BC24, respectively (Table

1). As the BC aerosol is removed from the atmosphere, the response gradually diminishes. The reduction in the global mean DSRF per unit mass of burden has not been maximized in the first two months when the global mean DSRF reduction reaches the maximum since the BC aerosol is still concentrated in the Northern Hemisphere (NH) (Fig. 2a inset and see description of Fig. 3a on BC interhemispheric transport). The efficiency of reduction is maximized in July of the first year as the BC is transported globally (see below). Doubling the BC injection from 12 to 24 Tg causes the reduction per Tg burden to decrease from –3.63 to –2.91 $\mathrm{W\,m^{-2}\,Tg^{-1}}$ in first year JJA (Table 1). After the first year, the surface DSRF reduction per Tg burden is comparable across all the cases. This indicates approximately a linear scaling of the surface DSRF reduction with the atmospheric burden of BC, which is expected for low-to-moderate forcing scenarios. Although the surface DSRF reduction per Tg burden is comparable across the scenarios, the BC burden decreases at a faster rate for the weaker forcing scenarios (Fig. 1b), resulting in a smaller surface DSRF reduction per Tg injection in the long term (Table 1). Comparing BC12 and BC24, the surface DSRF reduction per Tg injection for BC12 is initially comparable to that for BC24 but becomes only about half of the value for BC24 in years 6 to 15 (Table 1). This implies that by allowing more BC aerosol to reach the overworld, the stronger early-stage self-lofting effect in BC24 contributes to the reduction of DSRF at the surface in the long term. This translates to a nonlinear response in the long-term surface temperature response, as will be shown below.

| | DSRF | DSRF per Tg burden | DSRF per Tg injection | DLRF | DLRF per Tg burden | DLRF per Tg injection | TS | TS per Tg burden | TS per Tg injection |
|---|---|---|---|---|---|---|---|---|---|
| First year JF | -26.96 ± 2.38<br>(-14.80 ± 1.29) | -1.58 ± 0.26<br>(-1.77 ± 0.30) | -1.12 ± 0.10<br>(-1.23 ± 0.11) | +2.56 ± 1.03<br>(+1.65 ± 0.98) | +0.16 ± 0.07<br>(+0.21 ± 0.13) | +0.11 ± 0.04<br>(+0.14 ± 0.08) | -0.597 ± 0.077<br>(-0.389 ± 0.113) | -0.034 ± 0.004<br>(-0.046 ± 0.013) | -0.025 ± 0.003<br>(-0.032 ± 0.009) |
| First year JJA | -27.06 ± 1.19<br>(-13.09 ± 0.84) | -2.91 ± 0.06<br>(-3.63 ± 0.17) | -1.13 ± 0.05<br>(-1.09 ± 0.07) | +6.02 ± 0.49<br>(+6.36 ± 0.33) | +0.65 ± 0.07<br>(+1.78 ± 0.15) | +0.25 ± 0.02<br>(+0.53 ± 0.03) | -0.096 ± 0.087<br>(+0.356 ± 0.070) | -0.010 ± 0.009<br>(+0.101 ± 0.023) | -0.004 ± 0.004<br>(+0.030 ± 0.006) |
| Years 6-15 | -3.01 ± 0.89<br>(-0.78 ± 0.23) | -1.95 ± 0.19<br>(-2.40 ± 1.11) | -0.13 ± 0.04<br>(-0.07 ± 0.02) | -1.92 ± 0.30<br>(-0.46 ± 0.19) | -2.10 ± 0.87<br>(-3.42 ± 1.43) | -0.08 ± 0.01<br>(-0.04 ± 0.02) | -0.619 ± 0.047<br>(-0.172 ± 0.026) | -0.586 ± 0.163<br>(-0.919 ± 0.233) | -0.026 ± 0.002<br>(-0.014 ± 0.002) |

**Table 1.** Temporal means of the global responses of DSRF (in W m-2), DLRF (in W m-2), and surface temperature (TS; in °C) for BC24 (BC12 in brackets), with the 95% confidence intervals. The confidence intervals for the responses in years 6-16 are computed with lag-1 autocorrelation taken into account, assuming first-order autoaggressive dependence.

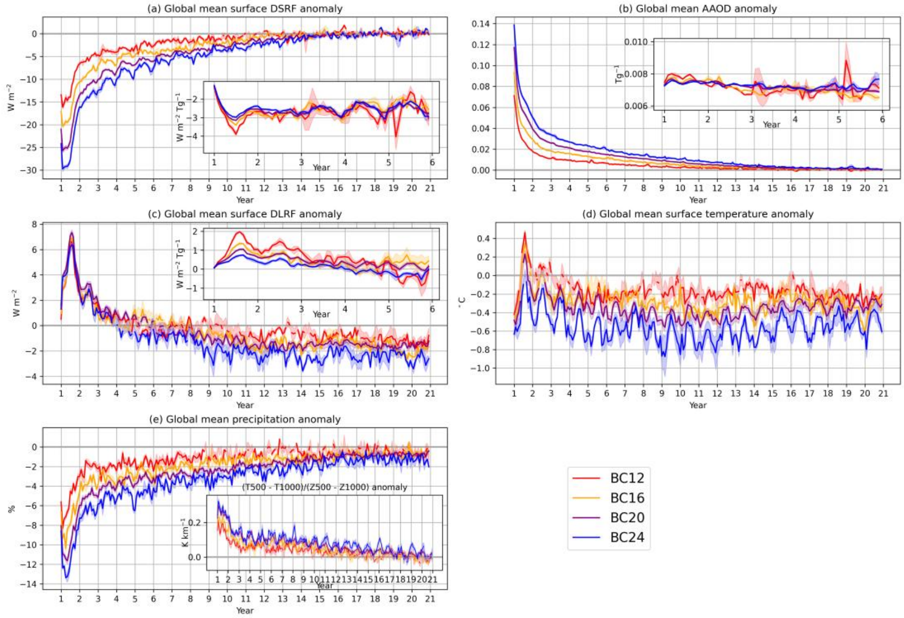

**Figure 2.** Monthly averaged global mean responses of (a) surface DSRF, (b) AAOD, (c) surface DLRF, (d) surface temperature, and (e) precipitation. Insets of (a) and (d) are the radiative flux responses divided by the atmospheric BC burden, respectively. Inset of (e) is the monthly averaged global mean responses of the temperature difference between 500 hPa and 1000 hPa, divided by the thickness of the column. Shading indicates the standard error of the mean. Dashed lines indicate where the standard error overlaps with the zero line.

The global mean aerosol absorption optical depth (AAOD) response is consistent with the surface DSRF response (Fig. 2b), also with an approximately linear scaling (Fig. 2b inset). Unlike the surface DSRF response, the AAOD response starts at its extremum since it depends on the relative radiant flux absorbed by the aerosol rather than the absolute change in the radiative flux. For our best-sampled simulation, BC20, the zonal mean AAOD ranges from 0.1 to 0.3 in most of NH in the first simulated year (Fig. 3a). The AAOD becomes comparable between the hemispheres after about 2 simulated years and is reduced to about 0.01-0.02 at high latitudes after 10 years.

In addition to the perturbation to shortwave radiative transfer, the longwave radiative transfer would also be perturbed by the aerosol injection due to changes in emissivity and thermal structure of the atmosphere (Ramaswamy & Kiehl, 1985). The surface downwelling longwave radiative flux (DLRF) response is initially negligible and then increases as the atmosphere is heated by the BC (Fig. 2c, 3b). For the best-sampled scenario, BC20, the global mean air temperature response exceeds 40 °C at 70 hPa in the first April following the injection and attains a maximum of 45 °C at 70 hPa few months later in June at the beginning of the boreal summer (Fig. 3b). The changes in longwave radiative transfer result in a global mean surface DLRF increase that peaks at +7.33 W m$^{-2}$ in August of the first year (Fig. 2c). The response in surface DLRF in first year JJA is similar among the different scenarios (Fig. 2c, Table 1). This implies that the surface DLRS increase per Tg burden in first year JJA is greater for the weaker forcing scenarios than the stronger forcing scenarios, in contrast to the approximate linearity of surface DSRF response (Fig. 2a,c insets, Table 1). In the long term, the positive response of surface DLRF decays faster than the negative response of surface DSRF (Fig. 2a,c).

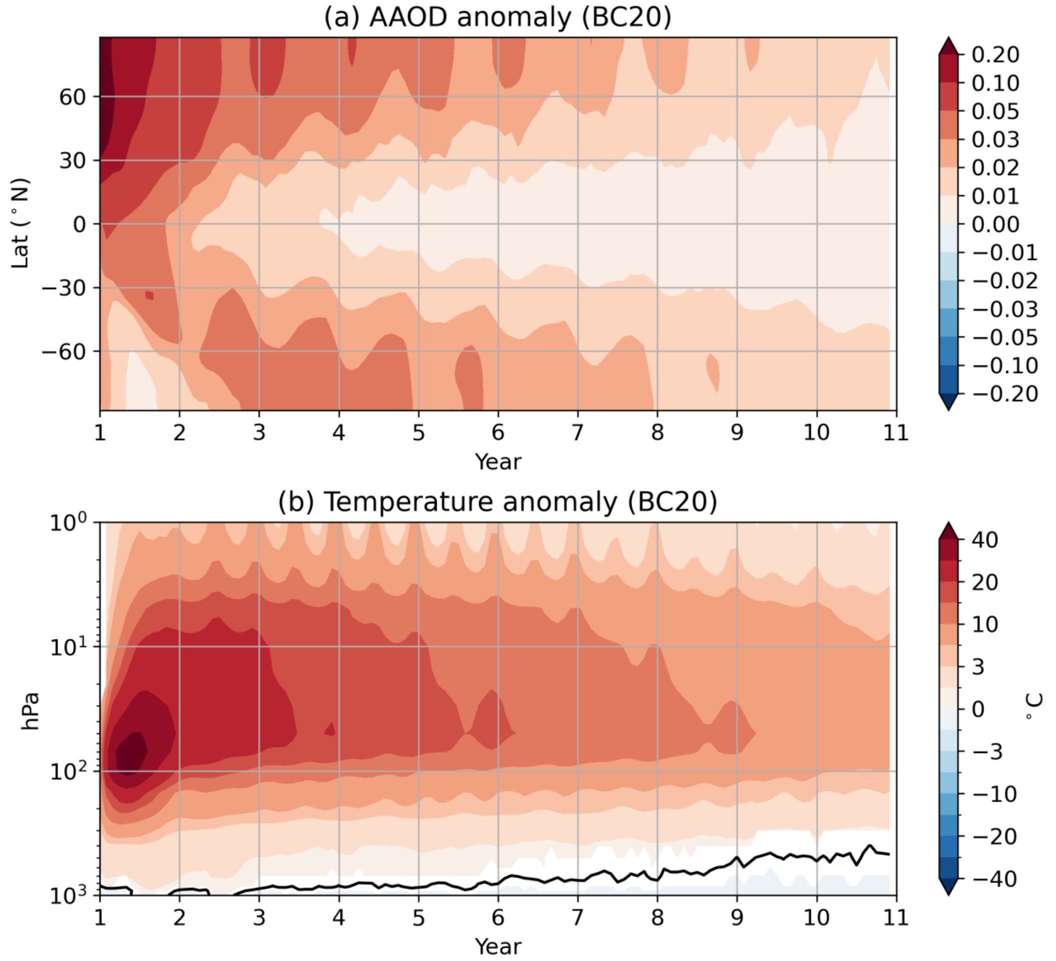

**Figure 3.** Monthly averaged responses of (a) zonal mean aerosol absorption optical depth at 550 nm and (b) horizontally averaged

air temperature. White patches indicate changes that are not significant at 95% confidence level using a t test. In (b), solid black line is the line of 0 K.

### 3.2 Impacts on global temperature and precipitation

The global mean surface temperature is decreased in response to the reduction in surface DSRF, but an unexpected oscillation is seen in the temperature response during the first boreal summer. The reduction in surface DSRF of –14.80 W m$^{-2}$ and –26.96 W m$^{-2}$ causes a rapid global mean surface cooling of –0.389 °C and –0.597 °C in first year JF for BC12 and BC24, respectively (Fig. 2d, Table 1). Surprisingly, instead of a gradual return to the climatological mean, the global mean surface temperature response increases drastically until it reaches a maximum in first year JJA. It is +0.356 °C and –0.096 °C for BC12 and BC24, respectively (Table 1). This implies that the global surface temperature response increases by more than 0.7 °C for BC12 from first year JF to JJA, whereas it increases by 0.5 °C for BC24 in the same period. The surface DLRF increase is consistent with the striking transient surface warming. It peaks at +6.36 W m$^{-2}$ and +6.02 W m$^{-2}$ in first year JJA, the same season in which the surface temperature response is at its highest (Fig. 2c,d, Table 1). After the temperature peak in first year JJA, the global mean surface temperature transitions back to a negative response and remains somewhat steady in years 6 to 15 before slowly returning to the climatological mean towards the end of the simulations (Fig. 2d). This is consistent with the trade-off between surface DSRF and DLRF, with the positive response of surface DLRF decaying faster than the negative response of surface DSRF (Fig. 2a,c). In years 6 to 15, the global mean surface temperature responses are –0.172 °C and –0.619 °C for BC12 and BC24 (Table 1). The surface temperature responses per Tg injection are –0.014 °C Tg$^{-1}$ and –0.026 °C Tg$^{-1}$. The nonlinear dependence of surface temperature response on the mass of injection is controlled by the nonlinear dependence of surface DSRF reduction on the mass of injection, -0.07 W m$^{-2}$ Tg$^{-1}$ and –0.13 W m$^{-2}$ Tg$^{-1}$ in years 6 to 15. As mentioned above, the stronger early-stage self-lofting effect in the stronger forcing scenarios contributes to the long-term surface DSRF reduction. Thus, the nonlinear self-lofting effect translates to a nonlinear response in the long-term surface temperature response.

Despite having surface temperature increase in the first boreal summer, the global mean precipitation response remains negative from the start to near the end of the simulations (Fig. 2e). While reduced precipitation is an expected part of the weakened hydrological cycle associated with nuclear winter (Robock et al., 2007a), the pronounced reduction of precipitation during the period of warming in the first year is consistent with the increase in static stability (Fig. 2e inset). The troposphere is stabilized as the upper troposphere is heated by the light-absorbing BC. This is clear from the best-sampled simulation, BC20 (Fig. 3b). Although the lower tropospheric response is a warming in the first boreal summer, the mid-tropospheric warming is greater. The greater static stability inhibits convection and reduces precipitation. The strongest vertical gradient of temperature response between 100 and 500 hPa emerges in the first year and is weakened afterward, but the sign of the temperature response gradient persists until the end of the simulated period, indicating a more stable troposphere throughout the simulation.

### 3.3 Spatial pattern of impacts on surface temperature

The regional pattern of surface temperature is forcing-dependent. Comparing the first year JJA responses between BC12 and BC24 reveals stronger polar cooling and larger sea ice expansion under higher forcing (Fig. 4). Moreover, mid-latitude warming is less intense in the higher forcing scenario. Although enhanced mid-tropospheric heating may increase DLRF, the stronger longwave effect under weaker forcing remain uncertain and is examined further below.

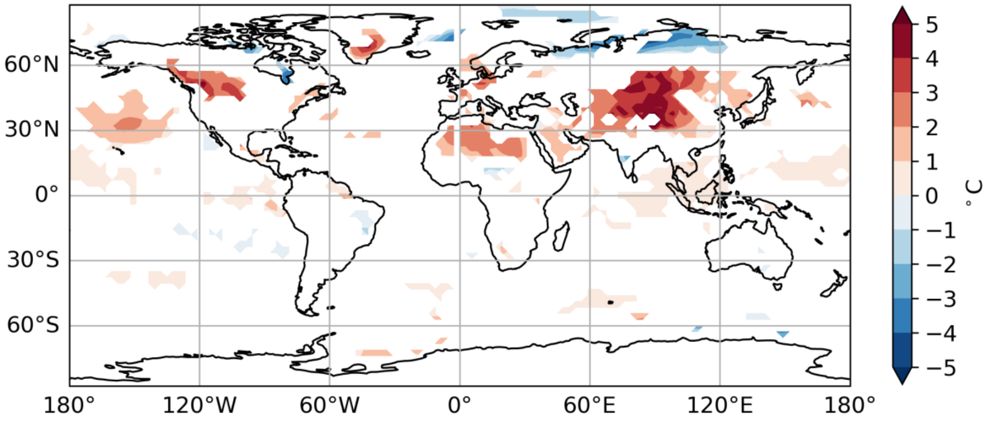
(a) Surface temperature anomaly (BC12; Year 1 JJA)

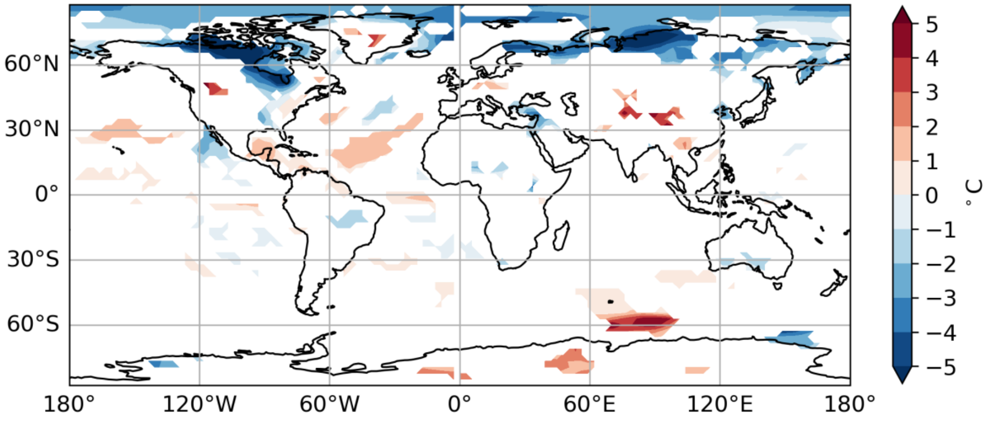
(b) Surface temperature anomaly (BC24; Year 1 JJA)

**Figure 4.** Responses of surface temperature for (a) BC12 and (b) BC24 in JJA of the first simulated year. White patches indicate changes that are not significant at 95% confidence level using a t test. The solid and dashed orange lines indicate the sea ice lines for the scenario and for the climatology, respectively. It is defined as the grids with 15% sea ice area.

https://doi.org/10.5194/egusphere-2025-5650
Preprint. Discussion started: 3 December 2025

To characterize this transient evolution from the initial year to subsequent years, we show the best sampled simulation, BC20, contrasting JF and JJA of the first year – marked by the pronounced surface temperature oscillation – with the quasi-steady response over years 6 to 15.

In the first two months following the injection, substantial surface cooling is seen on land as a result of the surface DSRF reduction. In NH, there is a statistically significant maximum cooling of about 8 °C in continental regions in the JF-mean (Fig. 5a). The reduction in surface DSRF causes most of the cooling, but the dynamical response likely contributed to some of the temperature responses. For example, the cooling around Greenland and the warming north of Siberia are likely due to a positive Arctic-Oscillation-like (AO) response (Fig. 5a; also see Fig. A1 for the regressed positive AO pattern in the control simulations; Stenchikov et al., 2002). A stronger AO-like response was shown for a 5 Tg India-Pakistan case by Robock et al. (2007b). In December to January (DJF) over years 6 to 15, the maximum cooling is at high latitudes, accompanied by sea-ice extent increase (Fig. 5b). This extends to a significant cooling of 2-3 °C in Europe and around 1.5 °C in southern Canada and the United States.

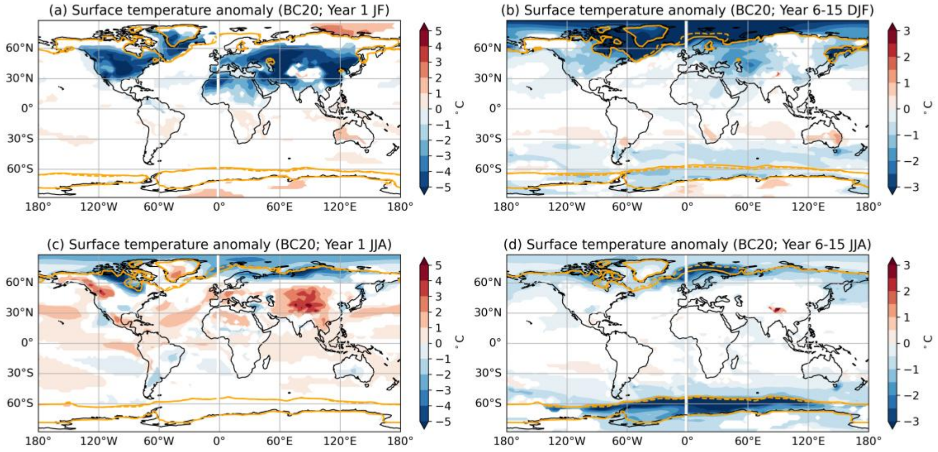

**Figure 5.** Responses of surface temperature as in Fig. 4 but for BC20 in (a) JF of the first year, (b) DJF of years 6-15, (c) JJA of the first year, and (d) JJA of years 6-15. White patches indicate changes that are not significant at 95% confidence level using a t test.

In the first boreal summer following the fire, substantial warming is seen in parts of Africa, North America, Greenland, and Tibet. A warming of up to +3-5 °C develops around Tibet, +2-3 °C in southern Greenland and the western North America, and +1-2 °C in northern Africa (Fig. 5c; and see Fig. 4 for the corresponding plots for BC12 and BC24). These areas are associated with relatively larger surface DLRF response (Fig. 6a). To better understand changes in the surface energy exchange, we calculated the surface net energy imbalance, which takes into account net shortwave radiative flux, net longwave radiative flux, sensible heat flux, and latent heat flux. The surface net energy imbalance is highly localized during the first boreal summer (Fig. 6b). For most land surfaces in NH, the net energy imbalance ranges from +2 to +5 W m$^{-2}$ (a positive sign corresponds to warming). Contributing to this positive response is not only a decrease in surface net longwave radiative flux (defined positive upward), but also a decrease in the turbulent fluxes as the atmospheric stability increases (turbulent fluxes not shown). Although the net energy imbalance is mostly negative for oceanic surface regions, especially at high latitudes, the higher heat capacity of ocean buffers the ocean surface temperature changes. The localized warming on land with adjustment by advection may result in the temperature response pattern and the positive global mean surface temperature response in the first boreal summer (Fig. 2c, 5c, A2). The long-term response for boreal summer shows statistically significant surface cooling mostly at high latitudes (Fig. 5d).

Overall, these simulations reveal a whipsaw effect on the surface temperature in the first year, where there is a quick transition from the very cold initial conditions to much warmer conditions over midlatitude land surfaces, and then a transition to strong mid-to-high latitude cooling as sea ice and ocean adjustments kick in.

https://doi.org/10.5194/egusphere-2025-5650
Preprint. Discussion started: 3 December 2025

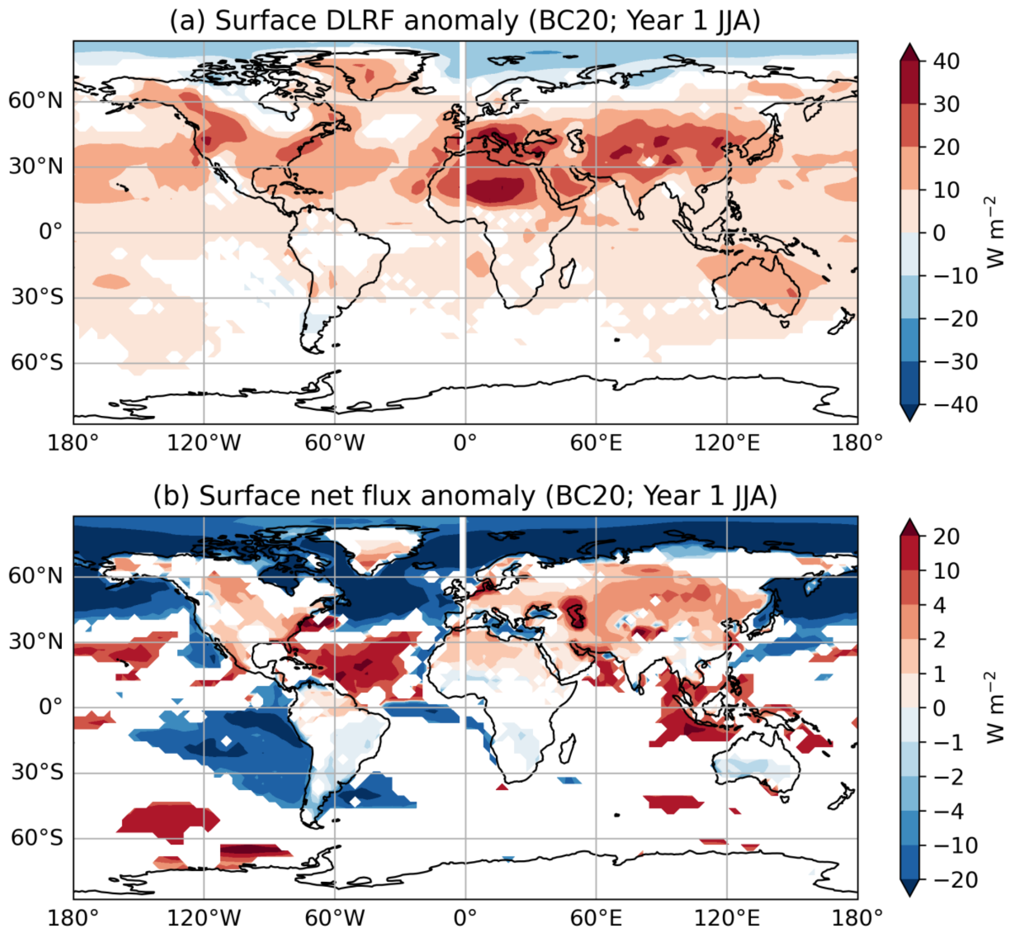

**Figure 6.** Responses of (a) surface DLRF, and (b) surface net flux in JJA of the first year for BC20. The surface net flux includes net shortwave radiative flux, net longwave radiative flux, latent heat flux, and sensible heat flux. The fluxes are defined as positive downward. White patches indicate changes that are not significant at 95% confidence level using a t test.

## 4 Discussions and conclusions

In this study, we explore the potential climate impacts of a hypothetical nuclear war between the United States and Russia, using a set of sensitivity studies with different low-to-moderate forcing scenarios using CanESM5. The forcing scenarios range from 12 to 24 Tg of BC injection at UTLS over the United States and Russia. We demonstrate, for the first time, the possibility of a transient global warming response in the first year following fire emissions in low-to-

https://doi.org/10.5194/egusphere-2025-5650
Preprint. Discussion started: 3 December 2025

moderate forcing nuclear war scenarios. The result highlights the nonlinear nature of the aerosol lifetime and thermal response, which can diverge substantially from those in strong-forcing cases.

During the first few months after injection, the global mean surface DSRF is drastically reduced, resulting in substantial global surface cooling, especially over NH land areas. Midway through the first year, however, a sign reversal occurs in the global mean surface temperature response, producing a transient warming before temperature returns to a negative response by year's end. This short-term warming is more pronounced under the weaker forcing scenario, where a larger fraction of BC remains in the lower atmosphere. The enhanced DLRF at the surface, together with reduced cooling via turbulent fluxes, contributed substantially to this warming. This signal is consistent with a stronger nighttime temperature increase (see Fig. A3 for daily minimum surface temperature and daily maximum surface temperature responses during year 1 JJA). The downwelling longwave enhancement likely stems from increased emissivity associated with tropospheric BC burden (Ramaswamy & Kiehl, 1985), although concurrent water vapor changes could also modulate radiative transfer. Further investigation into the sensitivity of the longwave response to the vertical smoke profile and varying water vapor content is warranted for the low-to-moderate forcing scenarios.

Absorbing particles above reflective surfaces can induce warming by absorbing shortwave radiation reflected from below and reemitting in the longwave (Bond et al., 2013). This may explain why the warming is mainly confined to dry, high-albedo regions such as Tibet, western North America, and northern Africa (see Fig. A4 for surface albedo in year 1 JJA). Although BC deposition slightly decreased surface albedo in these regions (not shown), the effect was too small to significantly influence DSRF. Moreover, a decreased albedo and greater shortwave absorption could not account for the simulated nighttime warming (Fig. A3; Kleidon & Renner, 2017).

The lifetime and transport of BC aerosol are key for understanding the resulting climate effects. In our low-to-moderate forcing scenarios, a larger initial injection led to a greater portion of BC reaching and persisting in the upper atmosphere due to enhanced self-lofting (Stenke et al., 2013). This nonlinear dependence of upper atmospheric burden on the initial injection is critical for the long-term climate response as aerosols in the upper atmosphere have longer lifetime. Hence, both the transient surface warming and the subsequent long-term cooling exhibit nonlinear dependence on injection mass. Our simulations show a faster removal rate compared to the previous studies: over two-thirds of the emitted BC is removed within the first simulated year, whereas other studies reported less than one-third removal for cases with a UTLS injection of 150 Tg over the United States and Russia and of 5 Tg over India and Pakistan (Coupe et al., 2019; Mills et al., 2014; Pausata et al., 2016; Robock et al., 2007b; Wagman et al., 2020). This may reflect the lower concentrations of BC in our 12-24 Tg injections compared to both 150 Tg United States-Russia and 5 Tg India-Pakistan cases. Additionally, model differences – such as aerosol coagulation treatment, gravitational settling, and model-top height – also affect the removal rate (Pausata et al., 2016; Coupe et al., 2019; Robock et al., 2007b). Future research should include systematic model intercomparisons to constrain these uncertainties.

The upper atmosphere experiences intense heating the absorbing BC. For BC20, the average temperature response at 200 hPa exceeds 15 °C midway through the first year (Fig. 3b). This is comparable to the temperature response at 200 hPa in the 150 Tg USA-Russia scenario (Coupe et al., 2019; Robock et al., 2007a). However, unlike those studies, our

https://doi.org/10.5194/egusphere-2025-5650
Preprint. Discussion started: 3 December 2025

zero-isotherm remained near the surface in the first few years, (Fig. 3b), likely because their injections were greater and occurred in May, whereas ours began in January. The temperature response at 200 hPa for BC20 also exceeds that in the 5 Tg India-Pakistan case from Mills et al. (2014) and Pausata et al. (2016). Although Mills et al. (2014) have reported that the choice of the initial season did not significantly affect the BC distribution or the climate impact for the 5 Tg India-Pakistan case, this may not be true for our 20 Tg USA-Russia case, which has initially less concentrated BC particles and less insolation in January. Also, for the same 5 Tg India-Pakistan scenario that starts the injection on January 1st, Pausata et al. (2016) found the temperature change to peak at 50 hPa 4 months after the injection in NorESM1-M (model top at 3 hPa), unlike the peak below 1 hPa at the beginning in CESM1-WACCM4 (model top at 5.1 x $10^{-6}$ hPa) from Mills et al. (2014). This indicates that the heating rate and vertical temperature structure depend strongly on the model configuration as well.

The climate effects on temperature and precipitation in our results are linked to impacts that warrant further study. The vertical structure of the warming enhances stability in the troposphere during the entire course of the simulation, which is coherent with the decreased precipitation (Fig. 2e inset). The long-term cooling is mainly confined to high latitudes and is not as drastic as the initial cooling in the midlatitudes. Together persistent cooling and reduced precipitation could still depress agricultural productivity (Xia & Robock, 2013; Xia et al., 2022). Conversely, the first-year transient warming occurs mostly over arid regions that are not major croplands and thus is unlikely to enhance yields. Instead, the warmer and drier surface conditions could heighten wildfire risk (Byrne et al., 2024).

OC is also a possible constituent of the smoke apart from BC. While OC is more short-lived and less absorbing in the visible range (Forrister et al., 2015), recent studies show that including OC can enhance surface cooling and stratospheric heating but reduce aerosol residence time by promoting coagulation (Pausata et al., 2016). We did not include OC emission in our scenarios, as our version of CanESM5.1 lacks coagulation processes. For further work, we will address this limitation using an updated version of CanESM with the Piecewise log-normal Aerosol Model (PAM; von Salzen, 2006), which allows for a more complete treatment of aerosol microphysics.

In summary, our simulations demonstrate, for the first time, the possibility of a transient global warming signal during the first year following fire emissions in low-to-moderate forcing nuclear war scenarios. This finding stands in contrast to the uniformly cooling response typically associated with strong-forcing nuclear winter events. The result highlights the nonlinear nature of the aerosol lifetime and thermal response, which can diverge substantially from those in strong-forcing cases. The warming arises from a complex balance between surface shortwave, longwave, and turbulent fluxes. While this longwave-driven warming is likely overwhelmed by surface shortwave reduction as the forcing increases and more BC aerosol is lofted into the stratosphere, its emergence here underscores the importance of model representations of aerosol microphysics and feedbacks involving turbulent heat exchange. The transient and spatially heterogeneous surface warming revealed in our simulations merits attention for its potential societal and environmental implications, even under relatively modest nuclear exchange scenarios.

## Appendix A

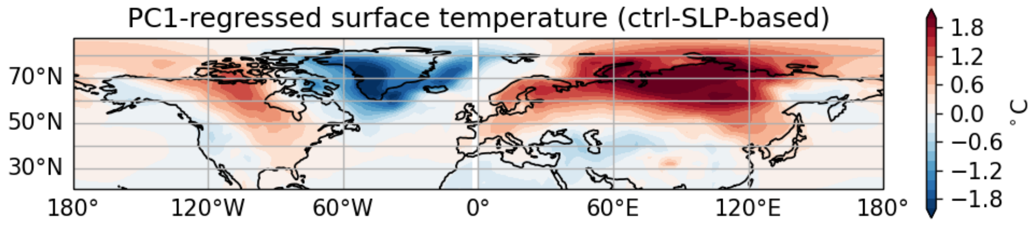
PC1-regressed surface temperature (ctrl-SLP-based)

**Figure A1.** The positive AO pattern in the control simulations, obtained by regressing surface temperature onto the first principal component (PC1) of sea-level pressure (SLP). 20°N-90°N daily zonal-mean SLP anomalies in DJF were used.

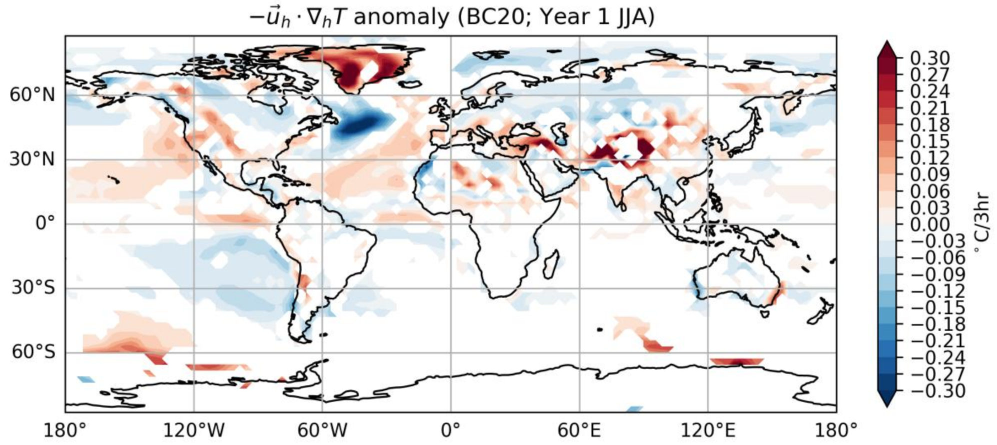
$-\vec{u}_h \cdot \nabla_h T$ anomaly (BC20; Year 1 JJA)

**Figure A2.** Temperature advection responses in JJA of the first year for BC20. The sign is defined such that positive values imply a positive local temperature tendency due to temperature advection. White patches indicate changes that are not significant at 95% confidence level using a t test.

https://doi.org/10.5194/egusphere-2025-5650
Preprint. Discussion started: 3 December 2025

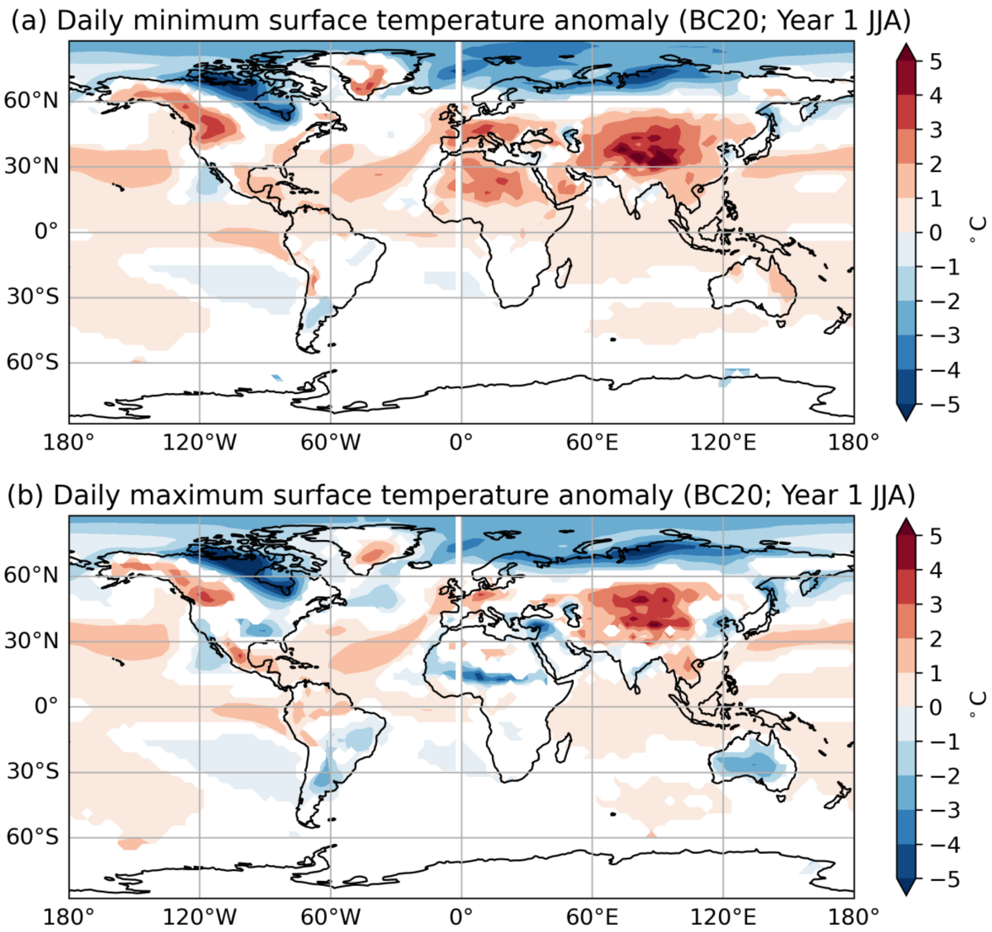

**Figure A3.** Responses of (a) daily minimum and (b) daily maximum surface temperature in JJA of the first year for BC20. White patches indicate changes that are not significant at 95% confidence level using a t test.

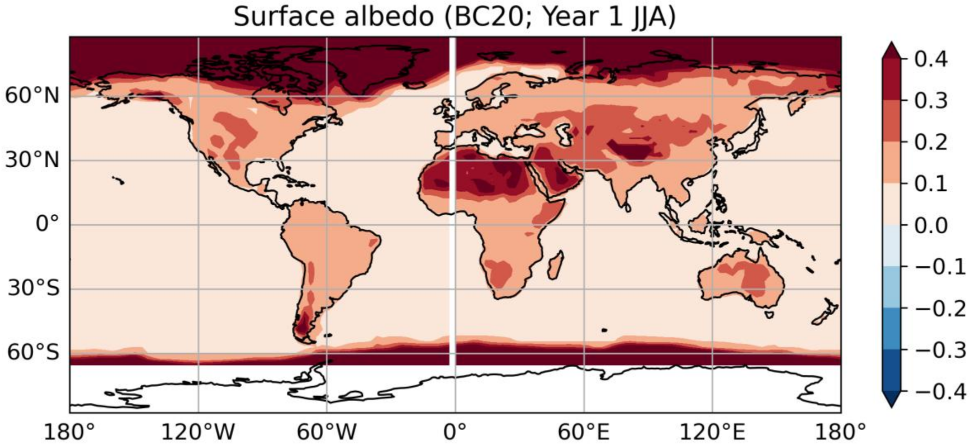

**Figure A4.** Surface albedo in JJA of the first year for BC20.

## Code and data availability

Both CanESM and the related tool imsi are released under the Open Government Licence Canada – 2.0. This license permits anyone to use or adapt them for lawful purposes, including commercial use, provided appropriate acknowledgement is given. Postprocessed output from the CanESM simulations, needed to reproduce the main figures, are publicly available on the University of Toronto Dataverse at https://doi.org/10.5683/SP3/UG2598. The full model outputs from the simulations are large and stored on the Trillium supercomputer at the SciNet HPC Consortium. Additional data from these simulations can be provided upon request by contacting Anson Cheung or Paul Kushner.

## Author contributions

PJK and FSRP coordinated the project and acquired financial support for the project; PJK and AKHC designed the simulations; AKHC adapted CanESM code and performed the simulations; AKHC analyzed the model output with contributions from all co-authors; AKHC wrote the manuscript draft; PJK, FSRP, ZZ, and MB reviewed and edited the manuscript.

## Competing interests

The authors declare that they have no conflict of interest.

## Acknowledgements

This work made use of resources provided by the Collaborative Platform for CanESM (CP4C). CP4C is supported by funding from Environment and Climate Change Canada (ECCC, Project Number GCXE25S055) and uses computational resources provided by SciNet and the Digital Research Alliance of Canada (RPP #1234 [RPP2025]). CanESM is a project of ECCC. The authors acknowledge Knut von Salzen and Jason N. S. Cole at ECCC for providing information about the existing model parameterizations and configurations.

## Financial support

This work has been supported by the Future of Life Institute (https://futureoflife.org/), project title "Constraining Nuclear War Fire Emissions and their Impacts on the Climate System".

## References

Bardeen, C. G., Kinnison, D. E., Toon, O. B., Mills, M. J., Vitt, F., Xia, L., Jägermeyr, J., Lovenduski, N. S., Scherrer, K. J. N., Clyne, M., and Robock, A.: Extreme ozone loss following nuclear war results in enhanced surface ultraviolet radiation, Journal of Geophysical Research: Atmospheres, 126(18), https://doi.org/10.1029/2021JD035079, 2021.

Bond, T. C., Doherty, S. J., Fahey, D. W., Forster, P. M., Berntsen, T., DeAngelo, B. J., Flanner, M. G., Ghan, S., Kärcher, B., Koch, D., Kinne, S., Kondo, Y., Quinn, P. K., Sarofim, M. C., Schultz, M. G., Schulz, M., Venkataraman, C., Zhang, H., Zhang, S., Bellouin, N., Guttikunda, S. K., Hopke, P. K., Jacobson, M. Z., Kaiser, J. W., Klimont, Z., Lohmann, U., Schwarz, J. P., Shindell, D., Storelvmo, T., Warren, S. G., and Zender, C. S.: Bounding the role of black carbon in the climate system: A scientific assessment. J. Geophys, Res. Atmos., 118, 5380-5552, doi:10.1002/jgrd.50171, 2013.

Byrne, B., Liu, J., Bowman, K. W., Pascolini-Campbell, M., Chatterjee, A., Pandey, S., Miyazaki, K., van der Werf, G. R., Wunch, D., Wennberg, P. O., Roehl, C. M., and Sinha, S.: Carbon emissions from the 2023 Canadian wildfires, Nature 633, 835-839, https://doi.org/10.1038/s41586-024-07878-z, 2024.

Cole, J. N. S., von Salzen, K., Li, J., Scinocca, J., Plummer, D., Arora, V., McFarlane, N., Lazare, M., MacKay, M., and Verseghy, D.: The Canadian Atmospheric Model version 5 (CanAM5.0.3), Geosci. Model Dev., 16, 5427-5448, https://doi.org/10.5194/gmd-16-5427-2023, 2023.

Coupe, J., Bardeen, C. G., Robock, A., and Toon, O. B.: Nuclear Winter Responses to Nuclear War Between the United States and Russia in the Whole Atmosphere Community Climate Model Version 4 and the Goddard Institute for Space Studies ModelE, Journal of Geophysical Research, Atmospheres, 124(15), 8522-8543. https://doi.org/10.1029/2019JD030509, 2019.

Croft, B., Lohmann, U., and von Salzen, K.: Black carbon ageing in the Canadian Centre for Climate modelling and analysis atmospheric general circulation model, Atmospheric Chemistry and Physics, 5, 1931-1949, 2005.

Dai, Y., Hitchcock, P., and Simpson, I. R.: What Drives the Spread and Bias in the Surface Impact of Sudden Stratospheric Warmings in CMIP6 Models? J. Climate, 37, 3917-3942, https://doi.org/10.1175/JCLI-D-23-0622.1, 2024.

Eyring, V., Bony, S., Meehl, G. A., Senior, C. A., Stevens, B., Stouffer, R. J., and Taylor, K. E.: Overview of the Coupled Model Intercomparison Project Phase 6 (CMIP6) experimental design and organization. Geoscientific Model Development, 9(5), 1937-1958, https://doi.org/10.5194/gmd-9-1937-2016, 2016.

Forrister, H., Liu, J., Scheuer, E., Dibb, J., Ziemba, L., Thornhill, K. L., Anderson, B., Diskin, G., Perring, A. E., Schwarz, J. P., Campuzano-Jost, P., Day, D. A., Palm, B. B., Jimenez, J. L., Nenes, A., and Weber, R. J.: Evolution of brown carbon in wildfire plumes, Geophys. Res. Lett., 42, 4623–4630, doi: 10.1002/2015GL063897, 2015.

Gettelman, A., Mills, M. J., Kinnison, D. E., Garcia, R. R., Smith, A. K., Marsh, D. R., Tilmes, S., Vitt, F., Bardeen, C. G., McInerny, J., Liu, H.-L., Solomon, S. C., Polvani, L. M., Emmons, L. K., Lamarque, J.-F., Richter, J. H., Glanville, A. S., Bacmeister, J. T., Phillips, A. S., Neale, R. B., Simpson, I. R., DuVivier, A. K., Hodzic, A., and Randel, W. J.: The whole atmosphere community climate model version 6 (WACCM6), Journal of Geophysical Research: Atmospheres, 124(23), 12380-12403, https://doi.org/10.1029/2019JD030943, 2019.

Ghan, S. J., Smith, S. J., Wang, M., Zhang, K., Pringle, K., Carslaw, K., Pierce, J., Bauer, S., and Adams, P.: A simple model of global aerosol indirect effects, Journal of Geophysical Research. Atmospheres, 118(12), 6688-6707, https://doi.org/10.1002/jgrd.50567, 2013.

Glasstone, S., Dolan, P. J., United States. Department of Defense, United States Department of Energy, and United States Defense Atomic Support Agency.: The effects of nuclear weapons (3rd ed.), U.S. Dept. of Defense, 1977.

Holton, J. R., Haynes, P. R., McIntyre, M. E., and Douglass, A. R.: Stratosphere-troposphere exchange, Rev. Geophys., 33, 403-439, https://doi.org/10.1029/95RG02097, 1995.

Johnson, B. T. and Haywood, J. M.: Assessing the impact of self-lofting on increasing the altitude of black carbon in a global climate model, Journal of Geophysical Research: Atmospheres, 128, https://doi.org/10.1029/2022JD038039, 2023.

Kleidon, A. and Renner, M.: An explanation for the different climate sensitivities of land and ocean surfaces based on the diurnal cycle, Earth System Dynamics, 8(3), 849-864, https://doi.org/10.5194/esd-8-849-2017, 2017.

Li, J., von Salzen, K., Peng, Y., Zhang, H., and Liang, X.: Evaluation of black carbon semidirect radiative effect in a climate model, Journal of Geophysical Research. Atmospheres, 118(10), 4715-4728, https://doi.org/10.1002/jgrd.50327, 2013.

Lohmann, U., von Salzen, K., McFarlane, N., Leighton, H. G., and Feichter, J.: Tropospheric sulfur cycle in the Canadian general circulation model, J. Geophys. Res., 104(D21), 26833-26858, doi:10.1029/1999JD900343, 1999.

Lucas, K. A., Orient J. M., Robinson A., Maccabee H., Morris P., Looney G., and Klinghoffer M.: Efficacy of bomb shelters: with lessons from the Hamburg firestorm, South Med J., 83(7), 812-820, doi: 10.1097/00007611-199007000-00022, 1990.

Madec, G. and the NEMO team: NEMO ocean engine, version 3.4, Institut Pierre-Simon Laplace Note du Pole de Modélisation 27, 367 pp, 2012.

Malone, R. C., Auer, L., Glatzmaier, G., Wood, M., and Toon, O. B.: Influence of solar heating and precipitation scavenging on the simulated lifetime of post-nuclear war smoke, Science, 230(4723), 317-319, https://doi.org/10.1126/science.230.4723.317, 1985.

Mills, M. J., Toon, O. B., Lee-Taylor, J., and Robock, A.: Multidecadal global cooling and unprecedented ozone loss following a regional nuclear conflict, Earth's Future, 2(4), 161-176, https://doi.org/10.1002/2013EF000205, 2014.

Mills, M. J., Toon, O. B., Turco, R. P., Kinnison, D. E., and Garcia, R. R.: Massive global ozone loss predicted following regional nuclear conflict, Proceedings of the National Academy of Sciences - PNAS, 105(14), 5307-5312, https://doi.org/10.1073/pnas.0710058105, 2008.

Namazi, M., von Salzen, K., and Cole, J. N. S.: Simulation of black carbon in snow and its climate impact in the Canadian Global Climate Model, Atmos. Chem. Phys., 15, 10887-10904, https://doi.org/10.5194/acp-15-10887-2015, 2015.

National Academies of Sciences, Engineering, and Medicine: Potential Environmental Effects of Nuclear War, Washington, DC: The National Academies Press, https://doi.org/10.17226/27515, 2025.

Ohneiser, K., Ansmann, A., Witthuhn, J., Deneke, H., Chudnovsky, A., Walter, G., and Senf, F.: Self-lofting of wildfire smoke in the troposphere and stratosphere: simulations and space lidar observations. Atmos. Chem. Phys., 23(4), 2901-2925, https://doi.org/10.5194/acp-23-2901-2023, 2023.

Pausata, F. S. R., Lindvall, J., Ekman, A. M. L., and Svensson, G.: Climate effects of a hypothetical regional nuclear war: Sensitivity to emission duration and particle composition, Earth's Future, 4(11), 498-511, https://doi.org/10.1002/2016EF000415, 2016.

Ramaswamy, V. and Kiehl, J. T.: Sensitivities of the radiative forcing due to large loadings of smoke and dust aerosols, J. Geophys. Res., 90(D3), 5597-5613, doi:10.1029/JD090iD03p05597, 1985.

Robock, A., Oman, L., and Stenchikov, G. L.: Nuclear winter revisited with a modern climate model and current nuclear arsenals: Still catastrophic consequences, Journal of Geophysical Research - Atmospheres, 112(D13), D13107-n/a, https://doi.org/10.1029/2006JD008235, 2007.

Robock, A., Oman, L., Stenchikov, G. L., Toon, O. B., Bardeen, C., and Turco, R. P.: Climatic consequences of regional nuclear conflicts, Atmospheric Chemistry and Physics, 7(8), 2003-2012, https://doi.org/10.5194/acp-7-2003-2007, 2007.

Samset, B. H., Wilcox, L. J., Allen, R. J., Stjern, C. W., Lund, M. T., Ahmadi, S., Ekman, A., Elling, M. T., Fraser-Leach, L., Griffiths, P., Keeble, J., Koshiro, T., Kushner, P., Lewinschal, A., Makkonen, R., Merikanto, J., Nabat, P., Narazenko, L., O'Donnell, D., Oshima, N., Rumbold, S. T., Takemura, T., Tsigaridis, K., and Westervelt, D. M.: East Asian aerosol cleanup has likely contributed to the recent acceleration in global warming, Commun Earth Environ, 6543, https://doi.org/10.1038/s43247-025-02527-3, 2025.

Scinocca, J. F., McFarlane, N. A., Lazare, M., Li, J., and Plummer, D.: Technical Note: The CCCma third generation AGCM and its extension into the middle atmosphere, Atmos. Chem. Phys., 8, 7055-7074, https://doi.org/10.5194/acp-8-7055-2008, 2008.

Shemwell, B. E. and Levendis, Y. A.: Particulates Generated from Combustion of Polymers (Plastics), Journal of the Air & Waste Management Association, 50(1), 94-102, https://doi.org/10.1080/10473289.2000.10463994, 2000.

Solomon, F. and Marston, R. Q.: The Medical Implications of Nuclear War, National Academy Press, 1986.

Stenchikov, G., Robock, A., Ramaswamy, V., Schwarzkopf, M. D., Hamilton, K., and Ramachandran, S.: Arctic Oscillation response to the 1991 Mount Pinatubo eruption: Effects of volcanic aerosols and ozone depletion, J. Geophys. Res., 107(D24), 4803, doi:10.1029/2002JD002090, 2002.

Stenke, A., Hoyle, C. R., Luo, B., Rozanov, E., Gröbner, J., Maag, L., Brönnimann, S., and Peter, T.: Climate and chemistry effects of a regional scale nuclear conflict, Atmospheric Chemistry and Physics, 13(19), 9713-9729, https://doi.org/10.5194/acp-13-9713-2013, 2013.

Swart, N. C., Cole, J. N. S., Kharin, V. V., Lazare, M., Scinocca, J. F., Gillett, N. P., Anstey, J., Arora, V., Christian, J. R., Hanna, S., Jiao, Y., Lee, W. G., Majaess, F., Saenko, O. A., Seiler, C., Seinen, C., Shao, A., Sigmond, M., Solheim, L., von Salzen, K., Yang, D., and Winter, B.: The Canadian Earth System Model version 5 (CanESM5.0.3), Geosci. Model Dev., 12, 4823-4873, https://doi.org/10.5194/gmd-12-4823-2019, 2019.

Tarshish, N. and Romps, D. M.: Latent heating is required for firestorm plumes to reach the stratosphere, Journal of Geophysical Research: Atmospheres, 127, https://doi.org/10.1029/2022JD036667, 2022.

Tewarson, A.: Chapter 4 Generation of Heat and Chemical Compounds in Fires, In P. J. DiNenno (Eds.), SFPE Handbook of Fire Protection Engineering (3rd ed., pp. 3-82--3-161), National Fire Protection Assoc, Inc. Quincy, Mass, 2002.

Toon, O. B., Turco, R. P., Robock, A., Bardeen, C., Oman, L., and Stenchikov, G. L.: Atmospheric effects and societal consequences of regional scale nuclear conflicts and acts of individual nuclear terrorism, Atmospheric Chemistry and Physics, 7(8), 1973-2002, https://doi.org/10.5194/acp-7-1973-2007, 2007.

Turco, R. P., Toon, O. B., Ackerman, T. P., Pollack, J. B., and Sagan, C.: Climate and Smoke: An Appraisal of Nuclear Winter, Science, 247(4939), 166-176, https://doi.org/10.1126/science.11538069, 1990.

von Salzen, K.: Piecewise log-normal approximation of size distributions for aerosol modelling, Atmospheric Chemistry and Physics, 6(5), 1351-1372, https://doi.org/10.5194/acp-6-1351-2006, 2006.

von Salzen, K., Scinocca, J. F., McFarlane, N. A., Li, J., Cole, J. N. S., Plummer, D., Verseghy, D., Reader, M. C., Ma, X., Lazare, M., and Solheim, L.: The Canadian Fourth Generation Atmospheric Global Climate Model (CanAM4). Part I: Representation of Physical Processes, Atmosphere-Ocean, 51(1), 104-125, https://doi.org/10.1080/07055900.2012.755610, 2013.

Wagman, B. M., Lundquist, K. A., Tang, Q., Glascoe, L. G., and Bader, D. C.: Examining the climate effects of a regional nuclear weapons exchange using a multiscale atmospheric modeling approach, Journal of Geophysical Research: Atmospheres, 125, https://doi.org/10.1029/2020JD033056, 2020.

Wood, R.: Drizzle in Stratiform Boundary Layer Clouds. Part II: Microphysical Aspects, Journal of the Atmospheric Sciences, 62(9), 3034-3050, https://doi.org/10.1175/JAS3530.1, 2005.

Wu, K., Li, J., von Salzen, K., and Zhang, F.: Explicit solutions to the mixing rules with three-component inclusions, Journal of Quantitative Spectroscopy & Radiative Transfer, 207, 78-82, https://doi.org/10.1016/j.jqsrt.2017.12.020, 2018.

Xia, L. and Robock, A: Impacts of a nuclear war in South Asia on rice production in Mainland China, Climatic Change, 116, 357-372, https://doi.org/10.1007/s10584-012-0475-8, 2013.

https://doi.org/10.5194/egusphere-2025-5650
Preprint. Discussion started: 3 December 2025

Xia, L., Robock, A., Mills, M., Stenke, A. and Helfand, I.: Decadal reduction of Chinese agriculture after a regional nuclear war, Earth's Future, 3(2), 37-48, https://doi.org/10.1002/2014EF000283, 2015.

Xia, L., Robock, A., Scherrer, K., Harrison, C. S., Bodirsky, B. L., Weindl, I., Jägermeyr, J., Bardeen, C. G., Toon, O. B., and Heneghan, R.: Global food insecurity and famine from reduced crop, marine fishery and livestock production due to climate disruption from nuclear war soot injection, Nat Food, 3, 586–596, https://doi.org/10.1038/s43016-022-00573-0, 2022.

Yu, P., Davis, S. M., Toon, O. B., Portmann, R. W., Bardeen, C. G., Barnes, J. E., Telg, H., Maloney, C., and Rosenlof, K. H.: Persistent Stratospheric Warming Due to 2019-2020 Australian Wildfire Smoke, Geophysical Research Letters, 48(7), https://doi.org/10.1029/2021GL092609, 2021.

Zanchettin, D., Khodri, M., Timmreck, C., Toohey, M., Schmidt, A., Gerber, E., Hegerl, G., Robock, A., Pausata, F., Ball, W., Bauer, S., Bekki, S., Dhomse, S., LeGrande, A., Mann, G., Marshall, L., Mills, M., Marchand, M., Niemeier, U., Poulain, V., Rozanov, E., Rubino, A., Stenke, A., Tsigaridis, K., and Tummon, F.: The Model Intercomparison Project on the climatic response to Volcanic forcing (VolMIP): experimental design and forcing input data for CMIP6, Geosci. Model Dev., 9, 2701-2719, https://doi.org/10.5194/gmd-9-2701-2016, 2016.